ACS Partner Journal

PRECISION CHEMISTRY

Editors' Choice

Open Access

pubs.acs.org/PrecisionChem

Article

Hydrogen Peroxide Electrosynthesis in a Strong Acidic Environment Using Cationic Surfactants

Zachary Adler, Xiao Zhang, Guangxia Feng, Yaping Shi, Peng Zhu, Yang Xia, Xiaonan Shan,* and Haotian Wang*

Cite This: https://doi.org/10.1021/prechem.3c00096

Read Online

ACCESS | Metrics & More | Article Recommendations | Supporting Information

ABSTRACT: The two-electron oxygen reduction reaction ($2e^-$-ORR) can be exploited for green production of hydrogen peroxide (H_2O_2), but it still suffers from low selectivity in an acidic electrolyte when using non-noble metal catalysts. Here, inspired by biology, we demonstrate a strategy that exploits the micellization of surfactant molecules to promote the H_2O_2 selectivity of a low-cost carbon black catalyst in strong acid electrolytes. The surfactants near the electrode surface increase the oxygen solubility and transportation, and they provide a shielding effect that displaces protons from the electric double layer (EDL). Compared with the case of a pure acidic electrolyte, we find that, when a small number of surfactant molecules were added to the acid, the H_2O_2 Faradaic efficiency (FE) was improved from 12% to 95% H_2O_2 under 200 mA cm^{-2}, suggesting an 8-fold improvement. Our in situ surface enhanced Raman spectroscopy (SERS) and optical microscopy (OM) studies suggest that, while the added surfactant reduces the electrode's hydrophobicity, its micelle formation could promote the O_2 gas transport and its hydrophobic tail could displace local protons under applied negative potentials during catalysis, which are responsible for the improved H_2O_2 selectivity in strong acids.

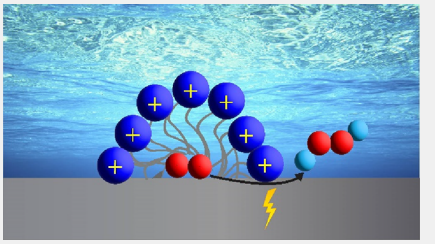

KEYWORDS: *electrocatalysis, hydrogen peroxide, electrosynthesis, oxygen reduction reaction, interfacial engineering, surfactant, CTAB*

INTRODUCTION

Hydrogen peroxide (H_2O_2), as one of the most important chemicals, is widely applied in paper and pulp manufacturing, disinfection, water treatment, and chemical synthesis.[1−3] The production and use of H_2O_2 has been increasing over the past several years,[4] and it has gained new attention due to the COVID-19 pandemic. Currently, H_2O_2 is mostly manufactured via the anthraquinone cycling process.[2,3] The cons of the anthraquinone process include high volumes of organic solvent and expensive noble metal catalyst utilization, large carbon footprint, expensive postsynthesis separations, and the installation of heavy infrastructure in centralized settings. In the past few decades, research has unveiled a more attractive method of H_2O_2 production, the electrosynthesis of H_2O_2 via the $2e^-$-ORR.[1,5−9] In the electrosynthesis process, renewable electricity can be employed to drive the reactions at ambient temperature, the emissions are environmentally benign, and the H_2O_2 can be produced in a decentralized manner without further separation processes. This $2e^-$ process differs from the traditional $4e^-$-ORR process, which generates H_2O in H_2/O_2 fuel cells. Catalyst selection is therefore important in order to steer the reaction toward the $2e^-$ path.[6] Many early works focused on noble metal and noble metal alloy catalysts,[10−13] though due to their high costs, more recent works have explored carbon-based materials as efficient catalysts for the $2e^-$ ORR, e.g., graphene, carbon nanotube (CNT), and amorphous carbon.[14−16]

Aside from catalyst selection, electrolyte selection is another critical factor in conducting H_2O_2 electrosynthesis. Alkaline electrolytes are preferred due to the superior selectivity toward H_2O_2 especially when using carbon-based catalysts,[7,11,12,14,15] but high-pH solutions also promote the H_2O_2 decomposition into HO_2^-.[5,17,18] In acidic solutions, the high concentration of protons at the electrode/electrolyte interface can easily lead to the hydrogen evolution reaction (HER) as well as the over-reduction of H_2O_2 to H_2O, both of which are undesirable since they decrease the H_2O_2 selectivity. These phenomena lead to a dilemma in which acid can help stabilize the generated H_2O_2, but alkaline environments can be more selective to H_2O_2 synthesis. In addition, the type of ion-exchange membrane is another factor that contributes to the application of acidic electrolyte. Proton-exchange membranes (PEMs) are required in acidic environments, and the most common PEM, Nafion, is very stable and commercially available. In contrast, anion-exchange membranes (AEMs), employed in alkaline environments, are not as reliable as PEMs. Some papers have reported high selectivity >90% FE H_2O_2 in acid electrolytes but only under current densities of a few milliamperes per centimeter

Received: September 23, 2023
Revised: December 8, 2023
Accepted: December 26, 2023

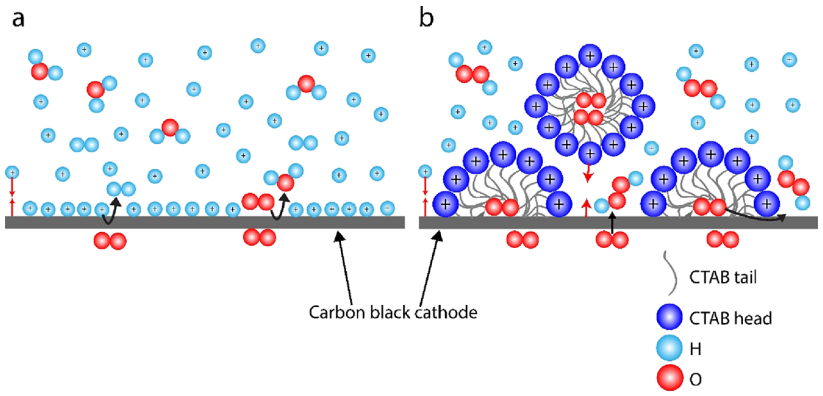

Figure 1. Schematic portraying the hypothetical EDL at the cathode interface (a) without CTAB and (b) with CTAB. H (cyan), CTAB tail (gray), CTAB head (blue), and O_2 (red).

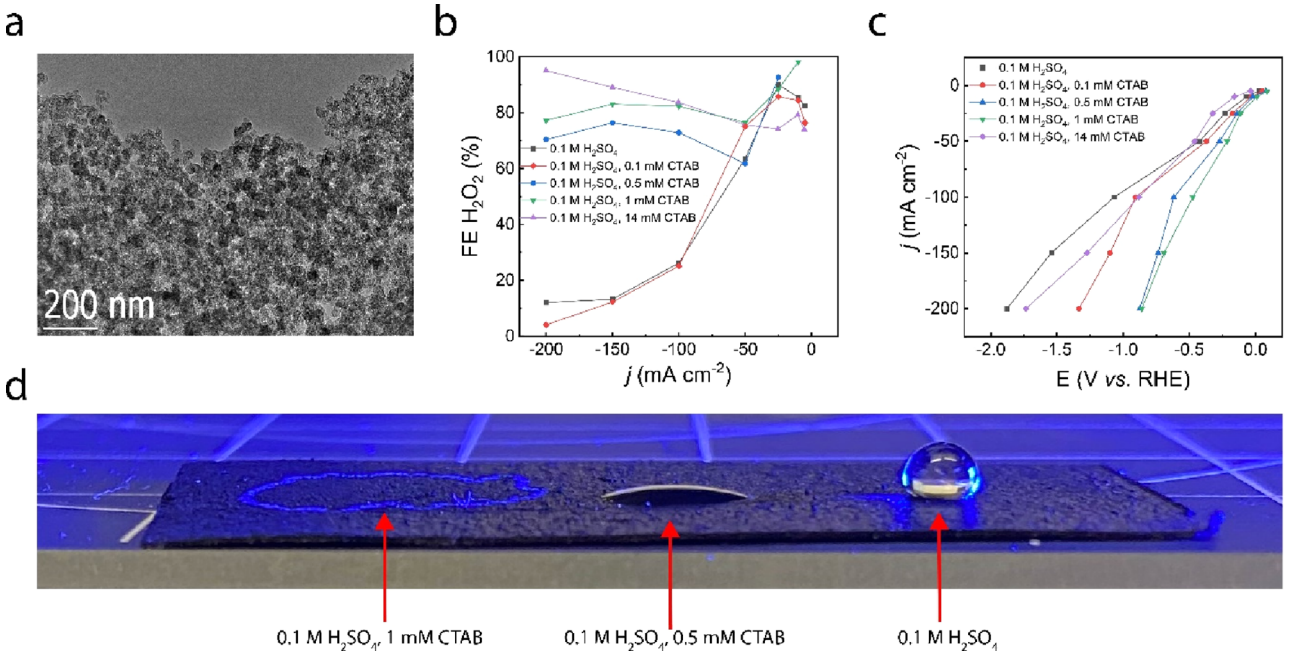

Figure 2. (a) TEM image of carbon black. Effect of CTAB concentration on (b) H_2O_2 selectivity and (c) electrocatalytic activity. (d) Contact angles of different electrolytes on the GDE.

squared.[10,13,19,20] For industrial applications, however, high current densities of several hundreds of milliamperes per centimeter square are necessary. Generally, higher current densities require larger overpotentials, at which the increased negative charge applied at the cathode will continuously attract protons to the surface, and thus make the system more susceptible to HER and the 4e$^-$-ORR. The selectivity−stability dilemma compels us to seek ways to influence the triple phase, gas−electrode−electrolyte, interface.

Inspired by biology, wherein micelles protect cells from the extracellular matrix, we propose utilizing amphiphilic surfactants to tune the hydrophobicity of the electrode−electrolyte interface and protect the electrode surface from the acidic bulk electrolyte.[21,22] Micelles in solution may have either or both of two effects (Figure 1): increased O_2 solubility and thus increased O_2 transport due to micellization[23] and a shielding effect that displaces protons from the EDL.[21,22,24] To demonstrate this idea, we added cetyltrimethylammonium bromide (CTAB, Figure S1a), a commonly used surfactant, to a strong acidic electrolyte (pH ∼ 1) to evaluate its impacts on the ORR selectivity of the carbon black catalyst. Carbon black catalyst has been demonstrated to show excellent H_2O_2 selectivity in alkaline electrolyte but poor selectivity in acidic solutions. However, when CTAB was added to the acidic electrolyte, the carbon black catalyst showed excellent H_2O_2 selectivity (>90%) under significant ORR current (>200 mA cm^{-2}). The enhancement effect from CTAB was also observed in the presence of other TAB surfactants, notably dodecyltrimethylammonium bromide (DTAB, Figure S1b) and hexyltrimethylammonium bromide (HTAB, Figure S1c). In situ SERS and in situ OM were applied to further investigate the surfactant effect. The SERS data reveals that CTAB interacts more strongly with the electrode at more negative potentials, which is reasonable given that TAB surfactants possess a positive charge. Additionally, in situ OM demonstrates that CTAB aggregates become immobilized as the reduction potential is increased. We attribute this effect to the adsorption of CTAB to the electrode surface. This study provides an interfacial engineering tool for enhancing H_2O_2 electrosynthesis as well as mechanistic insights into the

https://doi.org/10.1021/prechem.3c00096
Precis. Chem. XXXX, XXX, XXX−XXX

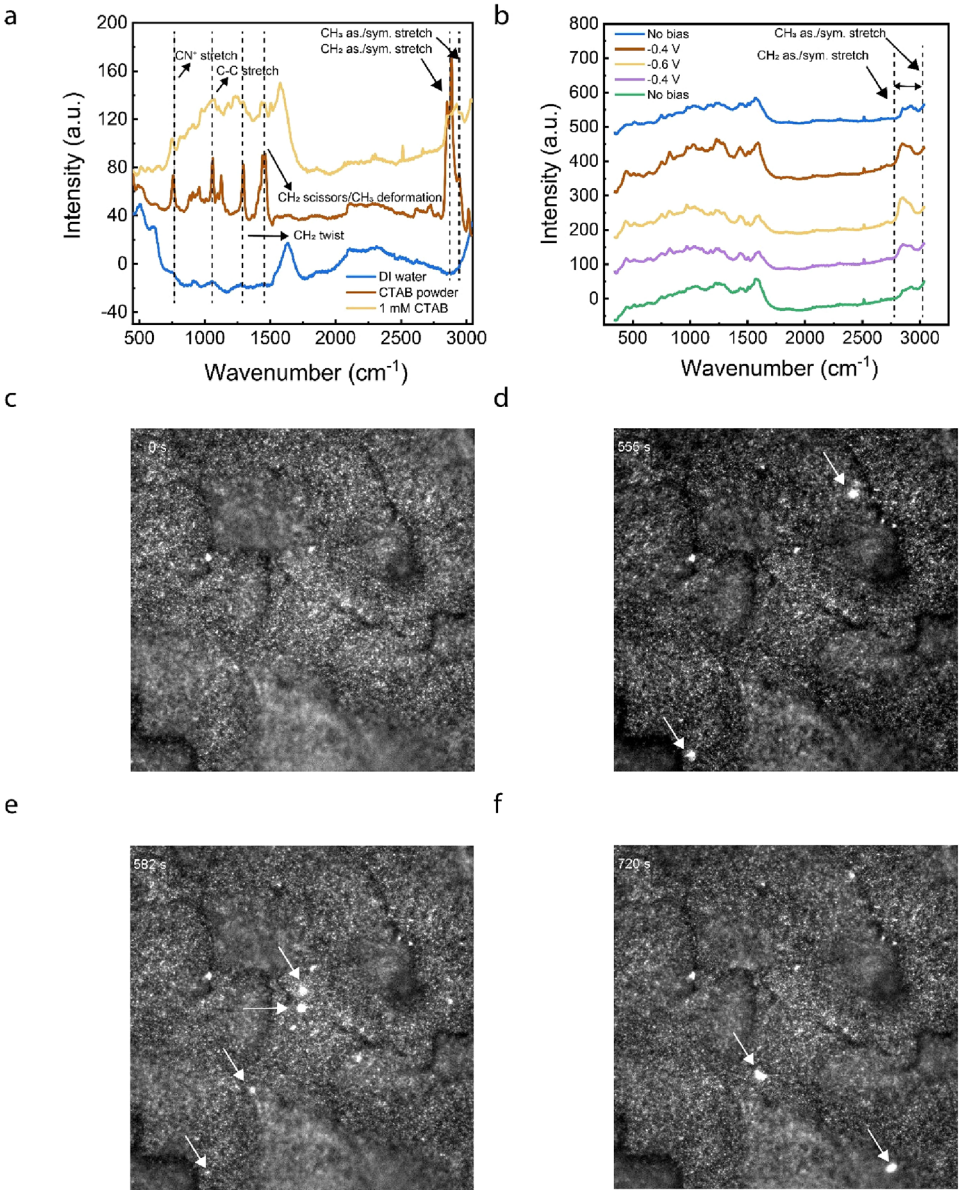

Figure 3. Raman spectroscopy data (a) of 0.1 M H_2SO_4 with 1 mM CTAB, CTAB powder, and DI water on Au foil with Au nanoparticle. Region 1 depicts CH_2 scissoring, twisting, and wagging. Region 2 depicts CH_2 stretching. (b) In situ SERS data at different potentials on Au foil with Au nanoparticles; (c–f) optical microscopy images of the CTAB micelle–electrode interactions at various timestamps during the activation process.

underlying phenomena. The new strategy proposed and demonstrated in this paper can be further applied to develop other interfacial engineering techniques that can be used to scale up our electrolyzers for more practical applications.

RESULTS

Electrochemical Reduction of O_2 to H_2O_2 in an Acidic Environment Using a Flow Cell

In order to measure the effects of the surfactant systems on $2e^-$-ORR, we carried out electrochemical measurements in a standard three-electrode flow cell with a saturated calomel electrode (SCE) as the reference electrode. Carbon black (BP2000) was chosen as the ORR catalyst due to its low cost and high selectivity (Figure 2a), while commercial IrO_2 was chosen as the anode catalyst. To maintain a low pH of ~1, we used 0.1 M H_2SO_4 as the electrolyte. At low overpotentials, the selectivity of H_2O_2 on carbon black was above 80%, achieving a maximum selectivity of 90% H_2O_2 at a current density of 25 mA cm^{-2} and a potential of −0.23 V vs RHE. However, by 100 mA cm^{-2} and −1.07 V vs RHE, the selectivity had already dropped to 26% in pure sulfuric acid solution. The drop in the H_2O_2 FE with increasing overpotential is expected, as the cathode would accumulate more negative charges, therefore attracting more protons to the electrode–electrolyte interface. We then added varying concentrations of CTAB to the electrolyte, noting that the critical micelle concentration (CMC), the concentration of surfactant required for micellization, is ~0.9 mmol L^{-1} (mM).[25,26] Figure 2b reveals that as the CTAB concentration increased so did the selectivity toward H_2O_2. Adding 0.5 mM CTAB to the electrolyte, for example, resulted in a selectivity of 76% FE H_2O_2 at a current density of 150 mA cm^{-2} and a potential of −0.74 V vs RHE, compared with 13% FE H_2O_2 without surfactant. With 1 mM CTAB added to the electrolyte, the FE further increased to 83% at 150 mA cm^{-2} under −0.69 V vs RHE. When 14 mM

https://doi.org/10.1021/prechem.3c00096
Precis. Chem. XXXX, XXX, XXX−XXX

CTAB was added to the electrolyte, the cell delivered a peak FE of 95% H_2O_2 at a current density of 200 mA cm^{-2} and a potential of −1.73 V vs RHE. We posit that CTAB displaces protons near the electrode surface, precluding the further reduction of H_2O_2 and the HER. CTAB could be directed toward the electrode surface due to the Coulombic interaction resulting from its positive charge and the negative charge of the electrode under reduction conditions.[27] Micellization of CTAB molecules could also help tune the hydrophobicity of the interface and favor H_2O_2 synthesis. To further confirm high H_2O_2 selectivities in the presence of CTAB, we measured the H_2 selectivity at the cathode outlet using gas chromatography (GC). As observed in Figure S2, we detected no observable H_2 peak, which would reflect a HER process occurring at the cathode. The only detectable peak was from unreacted O_2. Additionally, we observed that the activity increased with increasing CTAB concentration (Figure 2c), although this relation is not true for the 14 mM CTAB sample, which may have been too concentrated for favorable performance. At high surfactant concentrations, the gas diffusion layer (GDL) is susceptible to flooding, which may irreversibly damage the electrode. The activity relation demonstrates that the ORR kinetics are more sluggish in the absence of surfactant.

The O_2 transport depends on an aerophilic environment for fast and effective gas transport. In order to measure the hydrophobicity of the electrode−electrolyte interface, we calculated the contact angles of the electrolytes on the gas diffusion electrode (GDE) for varying concentrations of CTAB. As depicted in Figure 2d and Figure S3a and c, the contact angle of the pure acid electrolyte was 136°, compared with 68° in the presence of 0.5 mM CTAB and 0° in the presence of 1 mM CTAB. The 1 mM CTAB electrolyte clearly wets the GDE and can make the electrode more hydrophilic. At first glance, this result may appear to conflict with our electrochemical results, which reveal a high selectivity and activity of the 2-e^- ORR when CTAB is in solution. To compensate for the increased wetting of the GDE, we believe micellization could be a key factor for the increased O_2 concentration at the electrode−electrolyte interface,[23] in turn leading to higher activity and higher selectivity toward the H_2O_2 product. Thus, the increased hydrophilicity of the CTAB solution on the electrode surface does not have an adverse effect on the reaction, and the micelles are likely responsible for creating the aerophilic environment necessary for the ORR.

In Situ Experiments to Understand Behavior at the Electrode−Electrolyte Interface

We performed in situ Raman measurements to understand the interactions between the CTAB molecules and the electrode surface. To enhance the Raman signals, we deposited Au nanoparticles (50 nm in diameter) onto a Au electrode (50 nm Au on a glass substrate). The yellow curve in Figure 3a shows the Raman response of 1 mM CTAB in 0.1 M H_2SO_4 in the absence of electrolysis. For comparison, the Raman signal in DI water was also plotted (blue curve in Figure 3a). Two broad Raman band regions have been observed. The first region, which is at low wavenumbers (between 700 and 1600 cm^{-1}), includes CH_2 scissoring and CH_2 twisting/wagging modes.[28,29] The second region between 2800 and 3000 cm^{-1} corresponds to the C−H stretching mode of CTAB.[28−32] We also measured the Raman spectrum of CTAB powder (brown curve in Figure 3a), and the results reveal two broad Raman regions that are similar to those of the CTAB sample in solution (yellow curve in Figure 3a). This proves the observed Raman signal in the electrolyte is related to the CTAB molecules. Note that we see differences between the powder sample and the solution sample, which can be attributed to substrate effects and have been observed in other literature as well. In addition, the CTAB powder signals appear more intense compared with the respective signals in solution due to the higher concentration of the CTAB sample under the microscope. More importantly, the low frequency modes overlap with the strong substrate bands and are more difficult to resolve unambiguously.[28,29] Therefore, we use the C−H stretching modes (between 2800 and 3000 cm^{-1}) as the preferred region to detect and understand the CTAB−electrode interactions.

Figure 3b shows the Raman measurements conducted at different potentials in the 0.1 M H_2SO_4, 1 mM CTAB electrolyte. We started the experiment without any electric bias (blue curve in Figure 3b), and we clearly observed the C−H stretching mode of CTAB in the spectrum. This phenomenon indicates that the adsorption of CTAB onto the electrode surface can occur even in the absence of an electric potential. When we began to apply a negative potential (−0.4 V vs SCE, brown curve in Figure 3b), the intensity of the C−H stretching peak increased, indicating an enhanced adsorption of CTAB on the electrode surface. We believe this is due to the Coulombic attraction between the negatively charged electrode surface and the positively charged CTAB molecules. When the potential was further increased to −0.6 V vs SCE, the C−H stretching mode of CTAB increased again (yellow curve in Figure 3b). We then scanned the potential back to −0.4 V versus SCE (purple curve in Figure 3b), and the intensity of the peak decreased. Finally, the signal almost recovered to the original strength after the potential was removed (green curve in Figure 3b). This demonstration reveals that CTAB electrically adsorbs to the electrode surface under reduction potentials. While the adsorption strength is not too high to the point where CTAB irreversibly adheres, the CTAB adsorption does increase at larger overpotentials, providing insight into why the CTAB can help maintain a high H_2O_2 selectivity at large currents.

In a similar study, an optical microscope allowed us to visually observe the electrode−electrolyte interface directly on the carbon black electrode surface in real time. We used a transparent flow cell with 1 mM CTAB for visual purposes. Since the average size of a CTAB micelle is ∼5 nm in diameter,[33,34] it is impossible to detect the individual CTAB micelle using an optical microscope. To view the CTAB micelle and substrate interactions, we increased the micelle concentration and introduced relatively large micelle aggregates that could be observed with an optical microscope. The carbon electrode and catalyst absorbed most of the light, and the reflected light intensity was minimized. The individual CTAB aggregates could serve as scattering centers and show up as bright spots in the images (Supplementary Videos S1−S8). We imaged the electrode surface during the entire 20 min of the activation process (Supplementary Video S1). At the beginning of the activation, the electrode surface appeared relatively clean, and we did not observe any CTAB aggregates (Figure 3c). Within 13 min of activation, the bright CTAB aggregates began to attach to the electrode surface (pointed by the white arrows in Figure 3d−f). After activation, we recorded the electrode surface at different electric potentials (Supplementary Videos S2−S8). At no bias, 0, and −0.5 V vs SCE, we witnessed the CTAB aggregates freely moving around the

https://doi.org/10.1021/prechem.3c00096
Precis. Chem. XXXX, XXX, XXX−XXX

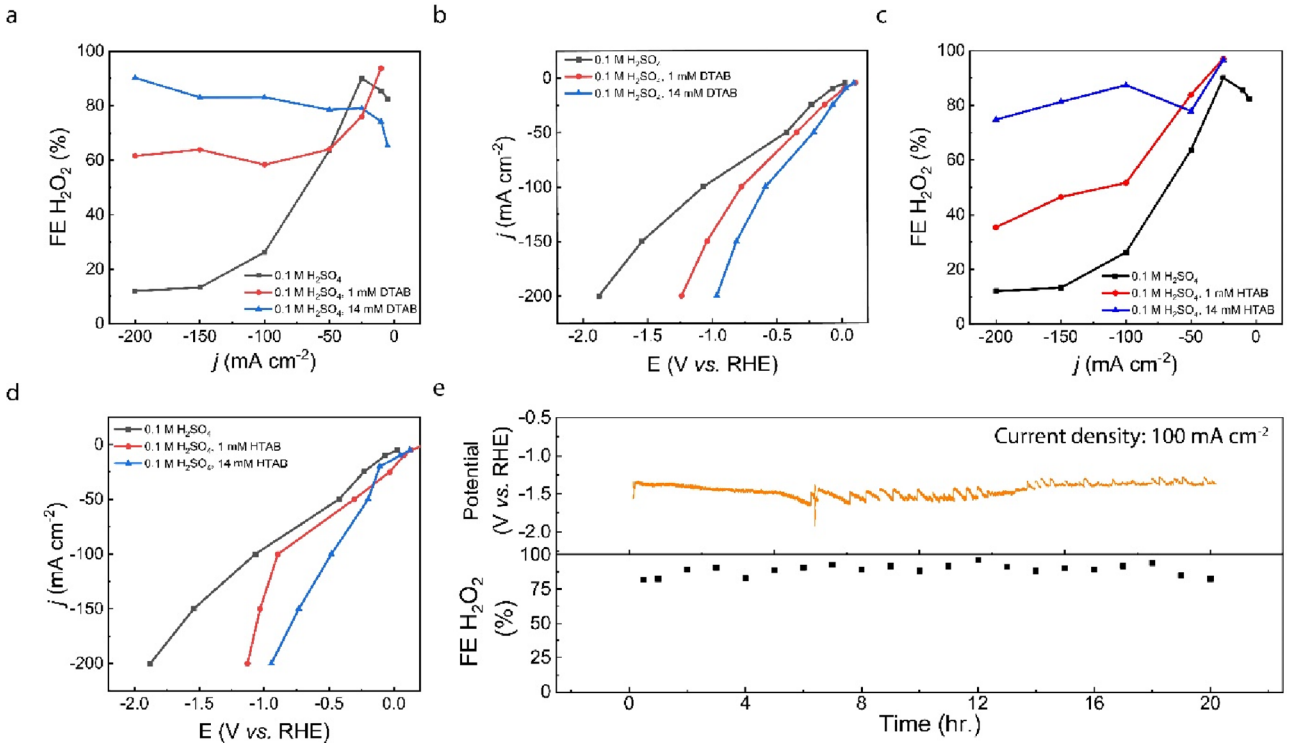

Figure 4. DTAB (a) H_2O_2 selectivity and (b) electrochemical activity. HTAB (c) H_2O_2 selectivity and (d) electrochemical activity. (e) Stability of 0.1 M H_2SO_4, 14 mm DTAB electrolyte in the flow cell. Current density was set to 100 mA cm^{-2}.

electrode surface and interacting with the electrode. At −1 and −2 V vs SCE, the CTAB aggregates moved toward the electrode and adhered to the electrode. At the same time, the CTAB aggregates were accumulated on the electrode surface. At −3 and −4 V vs SCE, there were almost no free CTAB aggregates in the imaging view, indicating the complete adhesion of CTAB to the electrode surface. The OM images provide strong and direct evidence to further support the idea that CTAB micelles adsorb onto the electrode surface, which would provide sufficient transport of the O_2 for 2e$^-$-ORR catalysis.

To ascertain how long the CTAB could remain on the electrode surface after electrochemical activation, we conducted a stability test, whereby, after activation at 150 mA cm^{-2} for 30 min, we switched the electrolyte from 1 mM CTAB in 0.1 M H_2SO_4 to the pure acid electrolyte (Figure S4) while continuing to monitor the H_2O_2 selectivity. The selectivity did not show an immediate drop to the performance level, which we observed in the pure acidic electrolyte test. In fact, the H_2O_2 FE remained above its value at 150 mA cm^{-2} in pure acid (13% FE H_2O_2) for over 2 h. With no continuous supply of surfactant solutions, we do not expect micellization to have had an impact on this lag in the drop in H_2O_2 selectivity. Instead, the effect can be attributed to CTAB molecules binding to the electrode surface, likely due to the negative charge of the cathode under electrolysis conditions.

Double Layer Capacitance Measurements

For stronger evidence of the ability of CTAB to displace protons at the EDL, we analyzed the double layer capacitance (C_{dl}) of the various electrolyte systems: pure H_2SO_4 and 0.5 and 1 mM CTAB in H_2SO_4. We calculated the C_{dl} from cyclic voltammetry curves (CVs) at varied scan rates (Figure S5a–d).[35] We measured the C_{dl} in the range of 0.4–0.5 V vs RHE due to this being a non-Faradaic (negligible reaction) potential range. The results demonstrate that C_{dl} decreases with increasing CTAB concentration. We postulate that the CTAB decreases the charge accumulation at the EDL due to the long, hydrophobic chains of the molecule that hinder ion transport. The CTAB molecules thus have an ability to tune the hydrophobicity near the electrode surface and increase the local pH. This decrease in charge accumulation agrees with our claim that, despite the CTAB increasing the degree of wetting of the electrode, the interfacial concentration of protons is reduced. Moreover, the electrochemical active surface area (ECSA)-normalized activity of the catalyst operating under various CTAB concentrations improves with increasing CTAB concentration (Figure S6). This observation reveals that, even after accounting for the differences in ECSA, the intrinsic activity is further enhanced in the presence of CTAB.

Extending the CTAB Effect to Other Surfactants

To confirm whether the enhancement effect from CTAB could be extended to other TAB surfactants, we compared electrochemical results from HTAB (CMC ∼ 1 M)[25] and DTAB (CMC ∼ 14 mM).[25,36] Whereas CTAB has a maximum alkyl chain length of 16 carbons, HTAB and DTAB have maximum alkyl chain lengths of 6 and 12, respectively. An electrolyte consisting of 14 mM DTAB yielded an H_2O_2 FE of 90% at a current density of 200 mA cm^{-2} and a potential of −0.967 V vs RHE, nearly 1 V less energy input than the pure acid electrolyte at the same current density with a 7.5-fold increase in selectivity (Figure 4a,b). While HTAB requires 1 M surfactant to form micelles, we observed significant Br_2 evolution while testing this highly concentrated electrolyte sample. The Br_2 evolution reaction can occur from the crossover of Br^- to the anode, which very large concentrations of TAB surfactants can induce. These concentrations are not

https://doi.org/10.1021/prechem.3c00096
Precis. Chem. XXXX, XXX, XXX−XXX

necessary, given that we can achieve >90% selectivity H_2O_2 with <0.02 M CTAB and DTAB. To illustrate this, we demonstrated that 14 mM HTAB could achieve 90% and 81% FE H_2O_2 at current densities of 100 and 150 mA cm^{-2}, respectively (Figure 4c). The trend of increased selectivity and activity with increased surfactant concentration holds for HTAB and DTAB, as it does for CTAB (Figure 4a–d). Thus, the surfactant effect is universal to all TAB surfactants, and some enhancement can still be achieved without micelles present in solution.

We excluded the counteranion effect on the enhanced H_2O_2 activity and selectivity by changing the surfactant from CTAB to cetyltrimethylammonium chloride (CTAC). CTAC has the exact same molecular structure as CTAB, except with Cl^- as the counteranion instead of Br^-. When CTAC was employed in our electrolyzer, a maximum H_2O_2 selectivity of 90% FE was achieved at 150 mA cm^{-2} and −0.75 V versus RHE (Figure S7). Finally, because industrial applications require long-term operation of electrochemical devices, we investigated the stability of the 14 mM DTAB electrolyte system. We chose this electrolyte sample due to its high H_2O_2 selectivity and high tolerance to GDE flooding. In the presence of 14 mM DTAB, the flow cell delivered >80% FE H_2O_2 for over 20 h (Figure 4e), revealing the high stability of the electrolyzer in the presence of surfactants.

■ CONCLUSION

This work demonstrates an interfacial engineering approach for the electrochemical generation of H_2O_2 in a strongly acidic environment. An 8-fold increase in the H_2O_2 selectivity at 200 mA cm^{-2} resulted in 95% FE H_2O_2 in the presence of 14 mM CTAB when compared with the pure acid solution. Furthermore, the reaction kinetics were improved with the addition of surfactants to the electrolyte, and we demonstrated high stability of the system over 20 h. In situ Raman spectroscopy and OM showed that CTAB particles adsorb onto the electrode surface during electrolysis, rendering a more aerophilic environment for O_2 transport, and in turn enhancing the H_2O_2 selectivity. C_{dl} measurements further confirmed the increased hydrophobicity and heightened pH with the addition of surfactants to the electrolyte, allowing for a selective $2e^-$-ORR process. While the results from this study are promising, more effort is required for this surfactant strategy to be implemented in the industrialization of acidic H_2O_2 electrosynthesis.

■ METHODS

Materials

CTAB and Nafion perfluorinated resin solution (527084-25 mL) were purchased from Sigma-Aldrich. HTAB and DTAB were purchased from TCI. Cerium sulfate ($Ce(SO_4)_2$) was purchased from Alfa Aesar. The sulfuric acid and methanol were from Millipore Corporation. Isopropanol was purchased from VWR Chemicals. Carbon black (BP2000) was purchased from Cabot Corporation.

Electrode Preparation

We prepared suspensions comprised of 40 mg of carbon black, 4 mL of 2-propanol, 1 mL of methanol, and 80 μL of Nafion binder. The suspension was sonicated in an ice bath for 30 min and then spray coated onto a 5 × 5 cm^2 GDL (Sigracet 28 BC, Fuel Cell Store) using an Air Brush. To dry the catalyst, we put the electrode in a vacuum chamber for 12 h. For use as a cathode in our flow cell, we then cut the GDE into 0.5 × 2 cm^2 pieces.

Electrolyte Preparation

We prepared varying concentrations of electrolytes of CTAB, HTAB, and DTAB by dissolving calculated amounts of the surfactants into 0.1 M H_2SO_4 solutions. For preparation of the 0.1 M H_2SO_4 solution, we mixed 2.72 mL of concentrated H_2SO_4 with 497 mL of Millipore H_2O (18.2 MΩ cm) for each 500 mL of electrolyte required.

Nafion 117 Membrane Activation

Nafion 117 membrane (Fuel Cell Store) was activated prior to electrochemical testing for the best results. In order to remove organic impurities, we heated the membrane at 80 °C in 5 wt % H_2O_2 for 1 h. We placed the membrane into H_2O again for 1 h at 80 °C to remove all residual H_2O_2. Next, we immersed the membrane in 1 M H_2SO_4 for 1 h at 80 °C to activate the membrane for H^+ crossover. Lastly, we placed the membrane in 80 °C water for 1 h to fully clean it.

Electrochemical Flow Cell Experiments

The flow cell utilized incorporated a saturated calomel electrode (SCE, CH Instruments) as the reference electrode. We used the following equation to convert experimental potentials versus SCE (E_{SCE}) into RHE (E_{RHE}): $E_{RHE} = E_{SCE} + 0.244 + 0.0591 \times pH$. The cell consisted of an IrO_2 anode (Fuel Cell Store) and a carbon black cathode, both 0.5 × 2 cm^2, with Nafion PEM in between. The catalyst layers on both electrodes faced the middle electrolyte flow channels. We flowed 30 sccm O_2 gas to the backside of the GDE via an Alicat Scientific mass flow controller (MFC). The catholyte and anolyte were both supplied to the cell via peristaltic pumps (Huiyu pump YZ15-13A), both operated at 2 rpm (~1.8 mL min^{-1}). We conducted all electrochemical experiments using a Biologic VMP3 workstation. We began the testing with resistance readings of the cell. This was conducted via a potentio electrochemical impedance spectroscopy (PEIS) measurement. The reported potentials in this study were all 80% compensated for the *iR* drop. After measuring the cell resistance, we carried out chronopotentiometry (CP) tests. We ramped the cell current up in 60 s steps: 1, 5, 10, 25, 50, and 100 mA to gradually ramp up the cell potential without damaging the electrode. After the energy reached 100 mA, we activated the catalyst for 20 min. Then, we returned the current to 5 mA, where we waited another 20 min before measuring the cell potential and collecting the H_2O_2 product for concentration measurement. This brief activation period ensured the maximum enhancement effect of the surfactant, as we noted small increases in selectivity during this time. The cathode outlet line was simultaneously rinsed well with DI water to remove highly concentrated H_2O_2. We measured selectivity and cell potential at the following currents: 5, 10, 25, 50, 100, 150, and 200 mA. All of the selectivity measurements reported are averages of two data points.

Quantification of H_2O_2 Concentration

For measuring the H_2O_2 concentration in the catholyte outlet stream, we exploited the reaction of Ce^{4+} with H_2O_2.

$$2Ce^{4+} + H_2O_2 \rightarrow 2Ce^{3+} + 2H^+ + O_2 \quad (1)$$

Ce^{4+} possesses a yellow color, while Ce^{3+} is colorless. We measured the Ce^{4+} concentration in a solution after reaction with the H_2O_2 product through use of a UV–vis spectrophotometer (UV-2600, Shimadzu).[14,15,37] Ce^{4+} has an absorption peak at ~317–319 nm. In order to react Ce^{4+} with H_2O_2, we combined 50 μL of H_2O_2-containing solution with 4 mL of 0.5 mM $Ce(SO_4)_2$. To maintain a stable $Ce(SO_4)_2$ solution, we dissolved $Ce(SO_4)_2$ in 0.5 M H_2SO_4. When H_2O_2 is dropped into 0.5 mM $Ce(SO_4)_2$, the solution loses some of its yellow color, making UV–vis detection an easy measure of Ce^{4+} concentration. We determined the Ce^{4+} concentration from a calibration curve based on 0.1, 0.2, 0.3, 0.4, and 0.5 mM $Ce(SO_4)_2$ solutions in 0.5 M H_2SO_4 (Figure S8). Then, we utilized eq 2 to determine the H_2O_2 concentration, based on the reaction in eq 1,

$$[H_2O_2] = \frac{4 \times [Ce^{4+}]_{initial} - 4.05 \times [Ce^{4+}]_{after}}{2 \times 0.05} \quad (2)$$

where all concentrations in brackets are in mmol L^{-1}. FE was then determined from eq 3

https://doi.org/10.1021/prechem.3c00096
Precis. Chem. XXXX, XXX, XXX–XXX

$$FE_{H_2O_2}(\%) = \frac{[H_2O_2] \times (\text{flow rate}) \times 2 \times 96{,}485}{I} \times 100\% \quad (3)$$

where I is the current in mA, the flow rate is in mL s^{-1}, 96,485 is the Faraday constant (C mol^{-1}), and the H_2O_2 concentration is in mol L^{-1}. This method was used for measuring the H_2O_2 concentration only for currents up to 150 mA, as we used the faster $KMnO_4$ titration method for currents above 150 mA. We explain why Ce^{4+} titration was required below.

The $KMnO_4$ titration is derived from the following chemical reaction:

$$2MnO_4^- + 5H_2O_2 + 6H^+ \rightarrow 2Mn^{2+} + 8H_2O + 5O_2 \quad (4)$$

We employed a standard $KMnO_4$ solution (0.1 N, Sigma-Aldrich), and 1 M H_2SO_4 was the H^+ source. The concentration of H_2O_2 in the product stream was determined based on the volumes of H_2O_2-containing solution and $KMnO_4$ at the titration end point, where the solution color turned from purple to clear. Equation 3 was then used for the selectivity calculation. While this titration method is faster and easier than the previous method, we found that at low currents, where low concentrations of H_2O_2 were generated, the surfactant in the electrolyte sample influenced the titration end point. The Ce^{4+} titration process, however, was not affected by the presence of a surfactant in solution.

Quantification of H_2 Gas

We measured the H_2 concentration using GC (Shimadzu GC-2014 GC).

Double Layer Capacitance Measurements

We conducted cyclic voltammetry (CV) experiments for measurement of C_{dl} of the electrode under various conditions. The bounds of the CV were 0.4 and 0.5 vs RHE, with a start and end point of 0.45 V. For each surfactant condition tested, we carried out 5 cycles of CVs. The following scan rates were used: 2, 4, 6, 8, and 10 mV s^{-1}.

In Situ Surface Enhanced Raman Spectroscopy and Optical Microscopy

For in situ SERS measurements, we dropped 50 nm-diameter Au nanoparticles on a Au foil electrode, which was then placed on a glass substrate so the laser could strike the sample. We dropped a 1 mM CTAB solution on top. The counter electrode was a Ag wire, and the reference electrode was the SCE. All electrodes were dipped into the electrolyte. The schematic of the home-built Raman microscopy system is shown in Figure S9. The home-built confocal Raman microscopy module was coupled with an inverted optical microscope (Olympus IX83). A diode laser beam at 642 nm (Vortran Stradus) was used to focus on the electrode surface and to excite the Raman scattering signal. The 20× water immersion objective (working distance: 2 mm, N.A. 1.0, Thorlabs) was applied to collect the Raman scattering signal and bright-field images. After separation with a spectrometer (iHR550, Horiba), the Raman signals were recorded by a charge-coupled device (CCD) for further analysis. We observed the Raman spectra from 500 to 3000 cm^{-1}.

For the OM videos, we constructed a transparent 3-electrode cell, again with Ag wire as the counter electrode and SCE as the reference electrode. The working electrode was the same as that in the electrochemical experiments with the flow cell, a GDE with carbon black coated on it. The cell contained one compartment, but we incorporated a divider to ensure no liquid electrolyte would contact the upward-facing backside of the GDE. The dry backside of the GDE ensured O_2 could penetrate the GDL. We transported O_2 to the backside of the GDE via a gas line, and all excess O_2 was free to disperse via an outlet gas line. A white light source (Thorlab) was used to illuminate the sample, and a scientific CMOS camera (Hamamatsu, C11440-42U30) was applied to record bright-field images and videos, with a spatial resolution of ∼300 nm.

■ ASSOCIATED CONTENT

Supporting Information

The Supporting Information is available free of charge at https://pubs.acs.org/doi/10.1021/prechem.3c00096.

Molecular structures, contact angles, UV−vis calibration curve, in situ microscopy schematic, and additional data (PDF)

Supplementary Video S1 - Electrode−electrolyte interface during the 20 min activation period (AVI)

Supplementary Video S2 - Electrode−electrolyte interface after the 20 min activation process (AVI)

Supplementary Video S3 - Electrode−electrolyte interface under 0 V vs SCE (AVI)

Supplementary Video S4 - Electrode−electrolyte interface under −0.5 V vs SCE (AVI)

Supplementary Video S5 - Electrode−electrolyte interface under −1 V vs SCE (AVI)

Supplementary Video S6 - Electrode−electrolyte interface under −2 V vs SCE (AVI)

Supplementary Video S7 - Electrode−electrolyte interface under −3 V vs SCE (AVI)

Supplementary Video S8 - Electrode−electrolyte interface under −4 V vs SCE (AVI)

■ AUTHOR INFORMATION

Corresponding Authors

Xiaonan Shan − *University of Houston, Department of Electrical and Computer Engineering, Houston, Texas 77004, United States;* orcid.org/0000-0001-7521-5573; Email: xshan@central.uh.edu

Haotian Wang − *Rice University, Department of Chemical and Biomolecular Engineering, Department of Chemistry, and Department of Materials Science and Nanoengineering, Houston, Texas 77005, United States;* orcid.org/0000-0002-3552-8978; Email: htwang@rice.edu

Authors

Zachary Adler − *Rice University, Department of Chemical and Biomolecular Engineering, Houston, Texas 77005, United States*

Xiao Zhang − *Rice University, Department of Chemical and Biomolecular Engineering, Houston, Texas 77005, United States;* orcid.org/0000-0002-4780-2161

Guangxia Feng − *University of Houston, Department of Electrical and Computer Engineering, Houston, Texas 77004, United States*

Yaping Shi − *University of Houston, Department of Electrical and Computer Engineering, Houston, Texas 77004, United States*

Peng Zhu − *Rice University, Department of Chemical and Biomolecular Engineering, Houston, Texas 77005, United States;* orcid.org/0000-0002-8855-0335

Yang Xia − *Rice University, Department of Chemical and Biomolecular Engineering, Houston, Texas 77005, United States*

Complete contact information is available at: https://pubs.acs.org/10.1021/prechem.3c00096

Author Contributions

Z.A., X.Z., and H.W. came up with the idea for the project and designed the experiments. Z.A. performed the experimental

https://doi.org/10.1021/prechem.3c00096
Precis. Chem. XXXX, XXX, XXX−XXX

work with some help and guidance from X.Z., Y.S., G.F., and X.S. Y.S., G.F., X.S., and Z.A. performed the in situ SERS experiments for the study. P.Z. and Y.X. provided guidance for some experiments. Z.A., G.F., H.W., and X.S. wrote the manuscript.

Notes

The authors declare no competing financial interest.

■ ACKNOWLEDGMENTS

This work was supported by the Robert A. Welch Foundation (grant no. C-2051-20230405), the David and Lucile Packard Foundation (grant no. 2020-71371), the Sloan Foundation (grant no. FG-2021-15638), and ACS PRF #62074-DNI5.

■ REFERENCES

(1) Yang, S.; Verdaguer-Casadevall, A.; Arnarson, L.; Silvioli, L.; Čolić, V.; Frydendal, R.; Rossmeisl, J.; Chorkendorff, I.; Stephens, I. E. L. Toward the Decentralized Electrochemical Production of H_2O_2: A Focus on the Catalysis. *ACS Catal.* **2018**, *8* (5), 4064−4081.

(2) Campos-Martin, J. M.; Blanco-Brieva, G.; Fierro, J. L. G. Hydrogen Peroxide Synthesis: An Outlook beyond the Anthraquinone Process. *Angew. Chem., Int. Ed.* **2006**, *45* (42), 6962−6984.

(3) Perry, S. C.; Pangotra, D.; Vieira, L.; Csepei, L.-I.; Sieber, V.; Wang, L.; Ponce de León, C.; Walsh, F. C. Electrochemical Synthesis of Hydrogen Peroxide from Water and Oxygen. *Nat. Rev. Chem.* **2019**, *3* (7), 442−458.

(4) *Bandwidth Study on Energy Use and Potential Energy Saving Opportunities in U.S. Chemical Manufacturing*; 2015, https://www.energy.gov/sites/prod/files/2015/08/f26/chemical_bandwidth_report.pdf.

(5) Jiang, Y.; Ni, P.; Chen, C.; Lu, Y.; Yang, P.; Kong, B.; Fisher, A.; Wang, X. Selective Electrochemical H_2O_2 Production through Two-Electron Oxygen Electrochemistry. *Adv. Energy Mater.* **2018**, *8* (31), No. 1801909.

(6) Siahrostami, S.; Verdaguer-Casadevall, A.; Karamad, M.; Deiana, D.; Malacrida, P.; Wickman, B.; Escudero-Escribano, M.; Paoli, E. A.; Frydendal, R.; Hansen, T. W.; Chorkendorff, I.; Stephens, I. E. L.; Rossmeisl, J. Enabling Direct H2O2 Production through Rational Electrocatalyst Design. *Nat. Mater.* **2013**, *12* (12), 1137−1143.

(7) Xia, C.; Xia, Y.; Zhu, P.; Fan, L.; Wang, H. Direct Electrosynthesis of Pure Aqueous H_2O_2 Solutions up to 20% by Weight Using a Solid Electrolyte. *Science* **2019**, *366* (6462), 226−231.

(8) Jiang, K.; Zhao, J.; Wang, H. Catalyst Design for Electrochemical Oxygen Reduction toward Hydrogen Peroxide. *Adv. Funct. Mater.* **2020**, *30* (35), No. 2003321.

(9) Zhang, X.; Xia, Y.; Xia, C.; Wang, H. Insights into Practical-Scale Electrochemical H2O2 Synthesis. *Trends Chem.* **2020**, *2* (10), 942−953.

(10) Jirkovský, J. S.; Panas, I.; Ahlberg, E.; Halasa, M.; Romani, S.; Schiffrin, D. J. Single Atom Hot-Spots at Au−Pd Nanoalloys for Electrocatalytic H_2O_2 Production. *J. Am. Chem. Soc.* **2011**, *133* (48), 19432−19441.

(11) Zheng, Z.; Ng, Y. H.; Wang, D.-W.; Amal, R. Epitaxial Growth of Au-Pt-Ni Nanorods for Direct High Selectivity H_2O_2 Production. *Adv. Mater.* **2016**, *28* (45), 9949−9955.

(12) Zhang, J.; Ma, J.; Choksi, T. S.; Zhou, D.; Han, S.; Liao, Y.-F.; Yang, H. B.; Liu, D.; Zeng, Z.; Liu, W.; Sun, X.; Zhang, T.; Liu, B. Strong Metal−Support Interaction Boosts Activity, Selectivity, and Stability in Electrosynthesis of H_2O_2. *J. Am. Chem. Soc.* **2022**, *144* (5), 2255−2263.

(13) Choi, C. H.; Kim, M.; Kwon, H. C.; Cho, S. J.; Yun, S.; Kim, H.-T.; Mayrhofer, K. J. J.; Kim, H.; Choi, M. Tuning Selectivity of Electrochemical Reactions by Atomically Dispersed Platinum Catalyst. *Nat. Commun.* **2016**, *7* (1), 10922.

(14) Lu, Z.; Chen, G.; Siahrostami, S.; Chen, Z.; Liu, K.; Xie, J.; Liao, L.; Wu, T.; Lin, D.; Liu, Y.; Jaramillo, T. F.; Nørskov, J. K.; Cui, Y. High-Efficiency Oxygen Reduction to Hydrogen Peroxide Catalysed by Oxidized Carbon Materials. *Nat. Catal.* **2018**, *1* (2), 156−162.

(15) Jiang, K.; Back, S.; Akey, A. J.; Xia, C.; Hu, Y.; Liang, W.; Schaak, D.; Stavitski, E.; Nørskov, J. K.; Siahrostami, S.; Wang, H. Highly Selective Oxygen Reduction to Hydrogen Peroxide on Transition Metal Single Atom Coordination. *Nat. Commun.* **2019**, *10* (1), 3997.

(16) Kim, H. W.; Ross, M. B.; Kornienko, N.; Zhang, L.; Guo, J.; Yang, P.; McCloskey, B. D. Efficient Hydrogen Peroxide Generation Using Reduced Graphene Oxide-Based Oxygen Reduction Electrocatalysts. *Nat. Catal.* **2018**, *1* (4), 282−290.

(17) Zhou, W.; Meng, X.; Gao, J.; Alshawabkeh, A. N. Hydrogen Peroxide Generation from O2 Electroreduction for Environmental Remediation: A State-of-the-Art Review. *Chemosphere* **2019**, *225*, 588−607.

(18) Qiang, Z.; Chang, J.-H.; Huang, C.-P. Electrochemical Generation of Hydrogen Peroxide from Dissolved Oxygen in Acidic Solutions. *Water Res.* **2002**, *36* (1), 85−94.

(19) Bu, Y.; Wang, Y.; Han, G.; Zhao, Y.; Ge, X.; Li, F.; Zhang, Z.; Zhong, Q.; Baek, J. Carbon-Based Electrocatalysts for Efficient Hydrogen Peroxide Production. *Adv. Mater.* **2021**, *33* (49), No. 2103266.

(20) Zhao, K.; Su, Y.; Quan, X.; Liu, Y.; Chen, S.; Yu, H. Enhanced H2O2 Production by Selective Electrochemical Reduction of O2 on Fluorine-Doped Hierarchically Porous Carbon. *J. Catal.* **2018**, *357*, 118−126.

(21) Banerjee, S.; Han, X.; Thoi, V. S. Modulating the Electrode−Electrolyte Interface with Cationic Surfactants in Carbon Dioxide Reduction. *ACS Catal.* **2019**, *9* (6), 5631−5637.

(22) Ge, W.; Chen, Y.; Fan, Y.; Zhu, Y.; Liu, H.; Song, L.; Liu, Z.; Lian, C.; Jiang, H.; Li, C. Dynamically Formed Surfactant Assembly at the Electrified Electrode−Electrolyte Interface Boosting CO_2 Electroreduction. *J. Am. Chem. Soc.* **2022**, *144* (14), 6613−6622.

(23) Hossain, Md. S.; Sahed, A.; Jahan, N.; Mollah, M. Y. A.; Susan, Md. A. B. H.; Islam, Md. M. Micelle Core as a Nest for Residence of Molecular Oxygen − An Electrochemical Study. *J. Electroanal. Chem.* **2021**, *894*, No. 115361.

(24) Zhang, X.; Zhao, X.; Zhu, P.; Adler, Z.; Wu, Z.-Y.; Liu, Y.; Wang, H. Electrochemical Oxygen Reduction to Hydrogen Peroxide at Practical Rates in Strong Acidic Media. *Nat. Commun.* **2022**, *13* (1), 2880.

(25) Oremusová, J. Micellization of Alkyl Trimethyl Ammonium Bromides in Aqueous Solutions−Part 1: Critical Micelle Concentration (CMC) and Ionization Degree. *Tenside Surfactants Deterg.* **2012**, *49* (3), 231−240.

(26) Goronja, J.; Janosevic-Lezaic, A.; Dimitrijevic, B.; Malenovic, A.; Stanisavljev, D.; Pejic, N. Determination of Critical Micelle Concentration of Cetyltrimethylammonium Bromide: Different Procedures for Analysis of Experimental Data. *Hem. Ind.* **2016**, *70* (4), 485−492.

(27) Wu, K.-H.; Wang, D.; Lu, X.; Zhang, X.; Xie, Z.; Liu, Y.; Su, B.-J.; Chen, J.-M.; Su, D.-S.; Qi, W.; Guo, S. Highly Selective Hydrogen Peroxide Electrosynthesis on Carbon: In Situ Interface Engineering with Surfactants. *Chem.* **2020**, *6* (6), 1443−1458.

(28) Dendramis, A. L.; Schwinn, E. W.; Sperline, R. P. A Surface-Enhanced Raman Scattering Study of CTAB Adsorption on Copper. *Surf. Sci.* **1983**, *134*, 675−688.

(29) Tyrode, E.; Rutland, M. W.; Bain, C. D. Adsorption of CTAB on Hydrophilic Silica Studied by Linear and Nonlinear Optical Spectroscopy. *J. Am. Chem. Soc.* **2008**, *130* (51), 17434−17445.

(30) Mathioudakis, G. N.; Soto Beobide, A.; Bokias, G.; Koutsoukos, P. G.; Voyiatzis, G. A. Surface-enhanced Raman Scattering as a Tool to Study Cationic Surfactants Exhibiting Low Critical Micelle Concentration. *J. Raman Spectrosc.* **2020**, *51* (3), 452−460.

(31) Joseph, D.; Rodriguez, R. D.; Verma, A.; Pousaneh, E.; Zahn, D. R. T.; Lang, H.; Chandra, S. Electrochemistry and Surface-Enhanced Raman Spectroscopy of CTAB Modulated Interactions of Magnetic Nanoparticles with Biomolecules. *RSC Adv.* **2017**, *7* (7), 3628−3634.

https://doi.org/10.1021/prechem.3c00096
Precis. Chem. XXXX, XXX, XXX−XXX

(32) Woods, D. A.; Petkov, J.; Bain, C. D. Surfactant Adsorption Kinetics by Total Internal Reflection Raman Spectroscopy. 2. CTAB and Triton X-100 Mixtures on Silica. *J. Phys. Chem. B* **2011**, *115* (22), 7353−7363.
(33) Dorshow, R.; Briggs, J.; Bunton, C. A.; Nicoli, D. F. Dynamic Light Scattering from Cetyltrimethylammonium Bromide Micelles. Intermicellar Interactions at Low Ionic Strengths. *J. Phys. Chem.* **1982**, *86* (13), 2388−2395.
(34) Patel, V.; Dharaiya, N.; Ray, D.; Aswal, V. K.; Bahadur, P. PH Controlled Size/Shape in CTAB Micelles with Solubilized Polar Additives: A Viscometry, Scattering and Spectral Evaluation. *Colloids Surf. Physicochem. Eng. Asp.* **2014**, *455*, 67−75.
(35) Wang, H.; Lu, Z.; Kong, D.; Sun, J.; Hymel, T. M.; Cui, Y. Electrochemical Tuning of MoS_2 Nanoparticles on Three-Dimensional Substrate for Efficient Hydrogen Evolution. *ACS Nano* **2014**, *8* (5), 4940−4947.
(36) Bruning, W.; Holtzer, A. The Effect of Urea on Hydrophobic Bonds: The Critical Micelle Concentration of n-Dodecyltrimethylammonium Bromide in Aqueous Solutions of Urea. *J. Am. Chem. Soc.* **1961**, *83* (23), 4865−4866.
(37) Sheng, H.; Hermes, E. D.; Yang, X.; Ying, D.; Janes, A. N.; Li, W.; Schmidt, J. R.; Jin, S. Electrocatalytic Production of H_2 O_2 by Selective Oxygen Reduction Using Earth-Abundant Cobalt Pyrite (CoS_2). *ACS Catal.* **2019**, *9* (9), 8433−8442.

https://doi.org/10.1021/prechem.3c00096
Precis. Chem. XXXX, XXX, XXX−XXX